High-resolution measurement, line identification, and spectral modeling of the $K\beta$ spectrum of heliumlike Ar^{16+}

P. Beiersdorfer, A. L. Osterheld, and T. W. Phillips
Lawrence Livermore National Laboratory, Livermore, California 94551

M. Bitter, K. W. Hill, and S. von Goeler
Princeton Plasma Physics Laboratory, Princeton, New Jersey 08543
(Received 27 February 1995)

High-resolution crystal spectrometer measurements of the $K\beta$ spectrum of heliumlike Ar^{16+} covering the wavelength region from 3.34 to 3.50 Å are presented and compared with detailed theoretical analyses. The measurements were made on the Princeton Large Torus tokamak and test the theoretical atomic data in the low-density limit at an electron density $n_e \leq 2\times10^{13}$ cm^{-3} and temperature $T_e = 2.3$ keV. Satellite transitions of the type $1s^2 2l$-$1s2l3l'$ and $1s^2 3l$-$1s3l3l'$ from lithiumlike Ar^{15+} and $1s^2 2l2l'$-$1s2l2l'3l''$ from berylliumlike Ar^{14+} are identified that are produced by either dielectronic recombination or electron-impact excitation. Good overall agreement between the predicted and measured intensities of the strong dielectronic satellites is found. The agreement demonstrates the utility of $K\beta$ spectra as a diagnostic of the electron temperature of low-density plasmas, such as those found in the Sun or magnetic fusion facilities. Poorer agreement is found for the weaker dielectronic satellite transitions, including the $1s3l3l'$ satellites that play an important role in the analysis of high-density plasma produced in laser fusion. Their intensity is underestimated by the calculations by about 50%. Moreover, it is shown that direct electron-impact excitation rates underestimate the relative intensity of the $1s^2\,{}^1S_0$–$1s2p\,{}^3P_1$ transition in heliumlike Ar^{16+} by a factor of 2, indicating the need for including additional excitation processes and possible blends with high-lying dielectronic satellites of the type $1s^2nl'$-$1s3lnl'$ with $n \geq 4$ in the theoretical models.

PACS number(s): 52.70.La, 32.30.Rj, 52.25.Nr, 52.25.Vy

I. INTRODUCTION

Electron temperatures of several thousand eV are routinely achieved in tokamak plasmas. As a result, mid-Z elements, such as argon, titanium, chromium, iron, and nickel, embedded as trace elements are typically found in the heliumlike charge state and radiate in the x-ray regime (1.5–4.0 Å). The heliumlike $K\alpha$ emission consisting of transitions from the $n=2$ levels to $n=1$ has been studied in detail on tokamaks (cf. references in [1]). These studies have demonstrated the great utility of the $K\alpha$ spectra for determining the plasma electron temperature, the ion transport coefficients, the fraction of non-Maxwellian electrons, the toroidal plasma rotation velocity, and the plasma ion temperatures. K-shell x-ray spectra involving transitions from levels higher than $n=2$ have been studied in much less detail. A measurement of the $K\gamma$ and $K\delta$ ($n=4,5$) spectra of heliumlike argon in the Alcator C tokamak have been reported by Källne *et al.* [2], and an analysis of spectra from very high-n levels in heliumlike argon was presented by Rice *et al.* [3].

To our knowledge only one detailed analysis of a heliumlike $K\beta$ spectrum ($n=3$ to $n=1$) recorded on a tokamak has been reported to date. Here, the $K\beta$ spectrum of Fe^{24+} was studied on the Tokamak Fusion Test Reactor (TFTR) tokamak [4]. It was shown that a detailed understanding of $K\beta$ spectra is crucial for accurate measurements of $K\alpha$ spectra, because in many cases the $K\beta$ radiation from one element tends to interfere with the $K\alpha$ radiation from another element with higher atomic number, provided both elements are present in the plasma. In particular, the $K\beta$ emission of heliumlike Fe^{24+} was shown to be in near coincidence with the $K\alpha$ emission of heliumlike Ni^{26+}. This interference is of particular importance because both iron and nickel are constituents of limiter and wall materials and thus coexist in many tokamak plasmas.

In contrast to the sparse attention received in tokamak measurements, $K\beta$ spectra from a variety of elements have been investigated in high-density plasma measurements, including the detailed analyses by Boiko *et al.* [5]. The spectra have become important spectral diagnostics of laser-produced plasmas in inertial confinement fusion (ICF) research [6,7]. The spectra are used for inferring the electron density and temperature of high-density plasmas generated in the core of imploding target capsules as well as for determining the mixing of pusher and fuel materials. For measurements of the fuel density and temperature, argon has been the element of choice because it is readily incorporated as a dopant ($\leq 0.2\%$) in the deuterium fuel and because heliumlike Ar^{16+} is copiously produced in plasmas generated at present-generation ICF facilities such as the NOVA laser facility [7]. The electron density of the fuel is inferred from the Stark-broadened profile of the $K\beta$ emission of heliumlike Ar^{16+}, which in contrast to the $K\alpha$ or Ly-α emission from heliumlike Ar^{16+} or hydrogenlike Ar^{17+}, respectively, is optically

TABLE I. Atomic parameters for transitions excited by electron impact. β_r denotes the branching ratio for $3\rightarrow 1$ radiative decay, and I denotes the relative line intensity at 2.3 keV. Wavelengths λ are given in Å.

Ion	Transition	Feature	β_r	I	λ_{theor}	λ_{expt}
Ar^{16+}	$(1s3p_{3/2})_1(^1P_1)\rightarrow$g.s.	$K\beta_1$	0.946	1.000	3.3654	3.3655
Ar^{16+}	$(1s3p_{1/2})_1(^3P_1)\rightarrow$g.s.	$K\beta_2$	0.172	0.023	3.3698	3.3696
Ar^{15+}	$(1s2s3p_{3/2})_{3/2}\rightarrow$g.s.	1	0.612	0.649	3.4044	3.4059
Ar^{15+}	$(1s2s3p_{1/2})_{3/2}\rightarrow$g.s.	1	0.751	0.410	3.4054	3.4059
Ar^{15+}	$(1s2p_{3/2}3p_{3/2})_{1/2}$ $\rightarrow(1s^22p_{1/2})_{1/2}$	2	0.193	0.007	3.4198	3.4193
Ar^{15+}	$(1s2s3p_{3/2})_{1/2}\rightarrow$g.s.	3	0.767	0.520	3.4216	3.4225
Ar^{15+}	$(1s2s3p_{3/2})_{3/2}\rightarrow$g.s.	3	0.742	1.000	3.4217	3.4225
Ar^{15+}	$(1s2p_{3/2}3p_{3/2})_{1/2}$ $\rightarrow(1s^22p_{3/2})_{3/2}$	3	0.309	0.011	3.4227	3.4225
Ar^{15+}	$(1s2s3p_{1/2})_{3/2}\rightarrow$g.s.	3	0.724	0.241	3.4234	3.4225
Ar^{15+}	$(1s2s3p_{1/2})_{1/2}\rightarrow$g.s.	3	0.684	0.093	3.4237	3.4225
Ar^{15+}	$(1s2s3d_{5/2})_{3/2}\rightarrow(1s^22p_{1/2})_{1/2}$	5	0.147	0.009	3.4426	3.4432
Ar^{15+}	$(1s2s3d_{5/2})_{5/2}\rightarrow(1s^22p_{3/2})_{3/2}$	6	0.135	0.013	3.4455	3.4460
Ar^{15+}	$(1s2s3s)_{1/2}\rightarrow(1s^22p_{1/2})_{1/2}$	7	0.014	0.006	3.4569	3.4574
Ar^{15+}	$(1s2s3s)_{1/2}\rightarrow(1s^22p_{3/2})_{3/2}$	8	0.022	0.010	3.4599	3.4608
Ar^{14+}	$(1s2s^23p_{3/2})_1(^1P_1)\rightarrow$g.s.	B	0.792	1.000	3.4655	3.466
Ar^{14+}	$(1s2s^23p_{1/2})_1(^3P_1)\rightarrow$g.s.		0.009	0.001	3.4711	

thin [6,7]. The fuel temperature is determined from the ratio of the $K\beta$ and Ly-β emission from Ar^{16+} and Ar^{17+}, respectively [7], or from the line shape of the Ar^{16+} $K\beta$ emission including neighboring dielectronic satellites from Ar^{15+} [8]. The diagnostic use of $K\beta$ spectra for such high-density plasma sources requires reliance on theoretical atomic physics parameters such as line positions, dielectronic resonance strengths, electron-impact excitation, and radiative rates. It is necessary, for example, to account for overlap with the emission from lithiumlike Ar^{15+} in order to infer the electron density from $K\beta$ emission of heliumlike Ar^{16+} [8,9]. In particular, lithiumlike satellite transitions of the type $1s2l3l'\rightarrow 1s^22l$ and $1s3l3l'\rightarrow 1s^23l$ need to be taken into account. These satellite transitions broaden the heliumlike $K\beta$ emission feature and would result in an overestimate of the density if ignored in modeling calculations [7–9]. A test of the atomic data is desirable to ascertain the reliability of the modeling calculations. Such a test can be accomplished by measuring spectra from plasmas with well-defined temperature and density, especially if nonspectroscopic methods are used to determine temperature and density.

In the following we present a detailed analysis of the $K\beta$ spectra of heliumlike Ar^{16+} recorded with a high-resolution crystal spectrometer on the Princeton Large Torus (PLT) tokamak. PLT plasmas are well diagnosed by nonspectroscopic techniques. The peak electron temperature is about 2.3 keV; the peak electron density does not exceed 2×10^{13} cm^{-3}. The spectral measurements thus test atomic theory in the low-density, so-called collisionless, limit. Our measurements include the positions and strengths of the $1s2l3l'\rightarrow 1s^22l$ and $1s3l3l'\rightarrow 1s^23l$ lithiumlike satellite lines populated by dielectronic recombination as well as transitions of the type $1s2l3l'\rightarrow 1s^22l$ excited by electron collisions. They also include satellite lines in berylliumlike Ar^{14+} of the type $1s2l2l'3l''\rightarrow 1s^22l2l'$. A detailed comparison of the measured argon spectrum with theoretical data is made and good agreement is obtained for the intensity of most dielectronic satellite transitions. An exception is given by the $1s3l3l'$ lithiumlike satellites. These were found to be 50% stronger than predicted. Moreover, it is shown that intensity estimates based solely on the electron-impact excitation of the heliumlike $1s3p$ levels underestimate the $K\beta_2$:$K\beta_1$ line ratio by a factor of 2 relative to the measured value. Calculated and measured line positions are generally in good agreement differing by no more than ± 2 mÅ.

The intensity of the dielectronic satellite lines relative to lines excited by electron impact is sensitive to the electron temperature. The temperature inferred from most ratios, involving either lithiumlike or berylliumlike dielectronic satellite lines, agrees within experimental uncertainties with the electron temperature determined by nonspectroscopic means. The good agreement demonstrates that the $K\beta$ emission from heliumlike ions can be used as a reliable electron temperature diagnostic for low-density plasmas. Since tokamak plasmas are in many respects similar to those of solar flares and the solar coro-

TABLE II. Rate coefficients for $1s$-$3p$ excitation of the $1s^2\,{}^1S_0$ ground state of heliumlike Ar^{16+}. Numbers in square brackets are powers of ten.

T_e (eV)	$(1s3p_{1/2})_1$ (cm^3/s)	$(1s3p_{3/2})_1$ (cm^3/s)
500	7.61[−16]	2.68[−15]
750	6.75[−15]	2.80[−14]
1000	1.88[−14]	9.00[−14]
1500	4.72[−14]	2.87[−13]
2000	6.95[−14]	5.13[−13]
2500	8.37[−14]	7.26[−13]
3000	9.19[−14]	9.16[−13]

TABLE III. Rate coefficients and threshold energies (in eV) for $1s$-$3p$ excitation of the $1s^22s$ ground state of lithiumlike Ar^{15+}. Numbers in square brackets denote powers of ten.

T_e (eV)	$(1s2p_{3/2}3p_{3/2})_{1/2}$ (cm^3/s)	$(1s2s3p_{3/2})_{3/2}$ (cm^3/s)	$(1s2s3p_{1/2})_{1/2}$ (cm^3/s)	$(1s2s3d_{5/2})_{5/2}$ (cm^3/s)	$(1s2s3d_{5/2})_{3/2}$ (cm^3/s)
500	3.32[−17]	8.72[−16]	4.38[−16]	7.33[−17]	4.82[−17]
750	3.37[−16]	8.67[−15]	4.38[−15]	7.32[−16]	4.82[−16]
1000	1.00[−15]	2.70[−14]	1.37[−14]	2.29[−15]	1.51[−15]
1500	2.97[−15]	8.27[−14]	4.23[−14]	7.15[−15]	4.72[−15]
2000	4.98[−15]	1.44[−13]	7.40[−14]	1.26[−14]	8.33[−15]
2500	6.70[−15]	2.00[−13]	1.03[−13]	1.77[−14]	1.17[−14]
3000	8.09[−15]	2.49[−13]	1.29[−13]	2.21[−14]	1.46[−14]
Threshold energy	3657.9	3641.9	3640.9	3633.9	3633.9

na, much of the analysis presented in this paper is applicable for the diagnosis of solar plasmas.

II. THEORY

Line radiation from highly charged ions in high-temperature, low-density tokamak or solar plasmas is produced by either electron-impact excitation or dielectronic recombination. In the $K\beta$ spectrum electron-impact excitation of the $1s^2\,{}^1S_0$ ground state in heliumlike ions populates the $1s3p$ levels, resulting in the resonance line $1s3p\,{}^1P_1 \rightarrow 1s^2\,{}^1S_0$, labeled $K\beta_1$, and the intercombination line $1s3p\,{}^3P_1 \rightarrow 1s^2\,{}^1S_0$, labeled $K\beta_2$. Electron-impact excitation of the lithiumlike and berylliumlike ground states populates the levels

$$1s^22s + e^- \rightarrow 1s2s3l + e^- \tag{1}$$

and

$$1s^22s^2 + e^- \rightarrow 1s2s^23l + e^- , \tag{2}$$

respectively. These levels may decay by autoionization or radiatively by either a $2\rightarrow1$ or $3\rightarrow1$ transition. The first type of radiative decay provides satellites to the heliumlike $K\alpha$ resonance line. These so-called $n=3$ satellites to the heliumlike $K\alpha$ resonance line have been investigated in detail for several different ions including Ar^{16+}, Ti^{20+}, Fe^{24+}, and Ni^{26+} [10–13]. The second type of radiative decay results in collisional satellites to the heliumlike $K\beta$ resonance line, and is of interest for the present study. Observation of the relative intensities of such collisional satellite lines provides a measure of the abundance of the different ionization states (e.g., [14]).

The emissivity ε_{DE} of a line excited by electron impact (direct excitation) is given by

$$\varepsilon_{DE} = n_e N_i \beta_r C , \tag{3}$$

where n_e and N_i are the electron and ion densities, β_r is the radiative branching ratio, and C is the excitation rate coefficient. To obtain the relative abundances N_i of different ionization stages from Eq. (3) the excitation rate coefficient C and radiative branching ratios β_r must be known for each transition. The excitation rate coefficients were obtained with the HULLAC set of atomic computer codes, which calculate wave functions, energy levels, and radiative transition rates by the relativistic, multiconfiguration parametric potential method with full configuration interaction [15]. The collisional excitation rates were calculated in the distorted-wave approximation; an efficient technique, which performs an angular factorization of both the direct and exchange contributions to excitation cross sections and interpolates the necessary radial integrals as a function of threshold energy was used [16]. The calculation of the radiative branching ratio requires knowledge of the autoionization rates. These were obtained from a factorization-interpolation technique using a single consistent potential for the bound and continuum orbitals [17]. The $2\rightarrow1$, $3\rightarrow1$, as well as the $3\rightarrow3$ radiative decay branches were included in the calculation of β_r. A listing of the atomic parameters of the transitions in heliumlike, lithiumlike, and berylliumlike argon excited by electron collisions is given in Table I. The rate coefficient for electron-impact excitation of the upper level of each transition is given for seven electron temperatures in Tables II, III, and IV for heliumlike, lithiumlike, and berylliumlike argon, respectively.

Dielectronic capture also contributes to features observed in a $K\beta$ spectrum. It populates doubly excited, autoionizing levels of the type $1s2l3l'$ in lithiumlike ions in the process

$$1s^2 + e^- \rightarrow 1s2l3l' . \tag{4}$$

The radiative decay of these levels contributes to the $K\beta$

TABLE IV. Rate coefficients for $1s$-$3p$ excitation of the $1s^22s^2\,{}^1S_0$ ground state of berylliumlike Ar^{14+}. Numbers in square brackets are powers of ten.

T_e (eV)	$(1s2s^23p_{1/2})_1$ (cm^3/s)	$(1s2s^23p_{3/2})_1$ (cm^3/s)
500	6.31[−16]	2.64[−15]
750	5.16[−15]	2.60[−14]
1000	1.37[−14]	8.15[−14]
1500	3.28[−14]	2.56[−13]
2000	4.65[−14]	4.57[−13]
2500	5.44[−14]	6.49[−13]
3000	5.83[−14]	8.20[−13]

TABLE III. (*Continued*).

T_e (eV)	$(1s2p_{3/2}3p_{3/2})_{1/2}$ (cm^3/s)	$(1s2s3p_{3/2})_{3/2}$ (cm^3/s)	$(1s2s3p_{1/2})_{1/2}$ (cm^3/s)	$(1s2s3d_{5/2})_{5/2}$ (cm^3/s)	$(1s2s3d_{5/2})_{3/2}$ (cm^3/s)
500	5.63[−16]	1.12[−15]	5.41[−16]	2.49[−16]	4.70[−16]
750	5.55[−15]	1.11[−14]	4.67[−15]	2.11[−15]	4.47[−15]
1000	1.72[−14]	3.44[−14]	1.29[−14]	5.73[−15]	1.34[−14]
1500	5.27[−14]	1.05[−13]	3.25[−14]	1.40[−14]	3.88[−14]
2000	9.18[−14]	1.83[−13]	4.85[−14]	2.03[−14]	6.41[−14]
2500	1.28[−13]	2.54[−13]	5.94[−14]	2.40[−14]	8.53[−14]
3000	1.59[−13]	3.16[−13]	6.64[−14]	2.61[−14]	1.02[−13]
Threshold energy	3623.6	3623.5	3621.7	3621.4	3619.0

spectrum in the form

$$1s2l3l' \rightarrow 1s^2 2l + h\nu \ . \tag{5}$$

Similarly, dielectronic capture excites levels of the type $1s2l2l'3l''$ in berylliumlike ions, which contribute to the $K\beta$ spectrum in the form

$$1s2l2l'3l'' \rightarrow 1s^2 2l2l' + h\nu \ . \tag{6}$$

Dielectronic recombination is a resonant process. Only those electrons whose energy E_{au} equals the difference of the binding energy of the $2l$ electron and of the energy $h\nu$ of the emitted x rays in Eq. (5) can recombine with the heliumlike ion in the ground state. This energy is about 2750 eV for dielectronic recombination with heliumlike argon. A similar energy is necessary for electrons recombining with lithiumlike argon to form the autoionizing levels in Eq. (6). Electrons with an energy of about 3300 eV are captured dielectronically into levels of the type $1s3l3l'$ in lithiumlike ions. These levels contribute to the $K\beta$ spectrum through radiative decay in the form

$$1s3l3l' \rightarrow 1s^2 3l + h\nu \ . \tag{7}$$

Capture into levels yet higher than $n=3$ are possible as well, populating levels such as $1s3lnl'$ with $n \geq 4$. This process leads to high-n satellites that blend with the heliumlike $K\beta$ resonance line and that cannot be resolved in our measurements. Such high-n satellite transitions are, therefore, not considered in our analysis.

The emissivity ε_{DR} of a lithiumlike satellite line excited by dielectronic recombination can be expressed as [18]

$$\varepsilon_{DR} = n_e N_{He} F_1(T_e) F_2(s) \ , \tag{8}$$

where the factor

$$F_1(T_e) = \frac{1}{2}\left[\frac{2\pi h}{mkT_e}\right]^{3/2} \exp(-E_{au}/kT_e) \tag{9}$$

depends only on the electron temperature, and the so-called line strength

$$F_2(s) = \frac{g_s}{g_i} A_a \beta_r \tag{10}$$

depends only on atomic parameters. Here A_a is the autoionization rate of the autoionizing level in the recombined ion, and g_s and g_i are the statistical weights of the autoionizing level and the ground state of the recombining ion, respectively. E_{au} is the energy difference of the

TABLE V. Atomic data for $1s3l3l'$ dielectronic satellite lines. Numbers in square brackets are powers of ten. Only lines with line strength $F_2 \geq 1.0\times10^{11}$ s^{-1} are listed.

Transition	E_{au} (eV)	λ_{theor} (Å)	F_2 (s^{-1})	Feature	λ_{expt} (Å)
$(1s3s3d_{3/2})_{5/2} \rightarrow (1s^2 3p_{3/2})_{3/2}$	3291.1	3.3689	1.75[11]		
$(1s3p_{3/2}3d_{5/2})_{3/2} \rightarrow (1s^2 3d_{5/2})_{5/2}$	3293.3	3.3692	1.02[11]		
$(1s3p_{3/2}3d_{3/2})_{5/2} \rightarrow (1s^2 3d_{3/2})_{3/2}$	3286.5	3.3751	1.50[11]		
$(1s3p_{1/2}3d_{5/2})_{7/2} \rightarrow (1s^2 3d_{5/2})_{5/2}$	3286.4	3.3755	2.07[11]		
$(1s3s3p_{3/2})_{3/2} \rightarrow (1s^2 3s)_{1/2}$	3263.9	3.3845	1.00[11]	*A*	3.3856
$(1s3s3p_{1/2})_{1/2} \rightarrow (1s^2 3s)_{1/2}$	3263.4	3.3849	2.15[11]	*A*	3.3856
$(1s3p_{3/2}3d_{5/2})_{7/2} \rightarrow (1s^2 3d_{5/2})_{5/2}$	3275.2	3.3858	2.34[12]	*A*	3.3856
$(1s3p_{3/2}3d_{3/2})_{5/2} \rightarrow (1s^2 3d_{3/2})_{3/2}$	3274.4	3.3863	1.31[12]	*A*	3.3856
$(1s3p_{3/2}3d_{5/2})_{5/2} \rightarrow (1s^2 3d_{5/2})_{5/2}$	3274.4	3.3866	2.15[11]	*A*	3.3856
$(1s3s3d_{5/2})_{3/2} \rightarrow (1s^2 3p_{1/2})_{1/2}$	3265.1	3.3920	3.88[11]		
$1s3p_{1/2}3p_{3/2})_{5/2} \rightarrow (1s^2 3p_{3/2})_{3/2}$	3265.0	3.3939	6.10[11]		
$(1s3s^2)_{1/2} \rightarrow (1s^2 3p_{1/2})_{1/2}$	3255.6	3.4009	1.02[11]		
$(1s3s^2)_{1/2} \rightarrow (1s^2 3p_{3/2})_{3/2}$	3255.6	3.4017	1.61[11]		

TABLE VI. Atomic data for $1s2s2l3l'$ dielectronic satellite lines excited in the capture of a free electron by lithiumlike ions in the $1s^22s$ ground state. Numbers in square brackets are powers of ten. Only lines with line strength $F_2 \geq 5.0\times10^{11}$ s^{-1} are listed.

Transition	E_{au} (eV)	λ_{theor} (Å)	F_2 (s^{-1})	Feature	λ_{expt} (Å)
$(1s2s2p_{3/2}3p_{3/2})_3\rightarrow(1s^22s2p_{3/2})_2$	2763.4	3.4557	6.56[13]		
$(1s2s2p_{1/2}3p_{3/2})_1\rightarrow(1s^22s2p_{1/2})_0$	2751.5	3.4643	6.15[11]	*B*	3.466
$(1s2s2p_{3/2}3p_{1/2})_2\rightarrow(1s^22s2p_{1/2})_1$	2752.1	3.4647	1.81[12]	*B*	3.466
$(1s2s2p_{3/2}3p_{3/2})_3\rightarrow(1s^22s2p_{3/2})_2$	2753.7	3.4650	3.57[12]	*B*	3.466
$(1s2s2p_{3/2}3p_{3/2})_0\rightarrow(1s^22s2p_{3/2})_1$	2775.8	3.4688	1.23[12]	*B*	3.466
$(1s2p_{1/2}2p_{3/2}3s_{1/2})_2\rightarrow(1s^22s2p_{3/2})_1$	2771.4	3.4730	1.87[12]		
$(1s2s2p_{1/2}3p_{3/2})_2\rightarrow(1s^22s2p_{3/2})_1$	2769.9	3.4745	1.39[13]		
$(1s2s2p_{3/2}3p_{3/2})_1\rightarrow(1s^22s2p_{1/2})_0$	2739.7	3.4758	6.25[11]		
$(1s2s2p_{3/2}3p_{3/2})_1\rightarrow(1s^22s2p_{3/2})_1$	2767.7	3.4767	1.82[12]		
$(1s2s2p_{1/2}3p_{3/2})_2\rightarrow(1s^22s2p_{1/2})_1$	2739.7	3.4767	1.89[12]		
$(1s2p_{1/2}^23s)_1\rightarrow(1s^22s2p_{3/2})_1$	2767.1	3.4772	1.47[12]		
$(1s2s2p_{3/2}3p_{3/2})_1\rightarrow(1s^22s2p_{3/2})_2$	2739.7	3.4787	4.31[12]		
$(1s2s2p_{1/2}3p_{3/2})_2\rightarrow(1s^22s2p_{1/2})_1$	2734.4	3.4819	1.55[13]	*C*	3.4831
$(1s2s2p_{3/2}3p_{3/2})_1\rightarrow(1s^22s2p_{1/2})_0$	2733.4	3.4820	6.91[12]	*C*	3.4831
$(1s2s2p_{3/2}3p_{3/2})_3\rightarrow(1s^22s2p_{3/2})_2$	2735.9	3.4824	3.48[13]	*C*	3.4831
$(1s2s2p_{3/2}3p_{3/2})_1\rightarrow(1s^22s2p_{3/2})_1$	2733.4	3.4829	7.31[12]	*C*	3.4831
$(1s2s2p_{1/2}3p_{3/2})_2\rightarrow(1s^22s2p_{3/2})_2$	2734.4	3.4839	8.99[12]	*C*	3.4831
$(1s2s2p_{3/2}3p_{3/2})_1\rightarrow(1s^22s2p_{3/2})_2$	2733.4	3.4849	5.93[11]	*C*	3.4831
$(1s2s2p_{1/2}3p_{1/2})_2\rightarrow(1s^22s2p_{3/2})_1$	2755.2	3.8489	2.51[12]	*C*	3.4831
$(1s2s2p_{3/2}3d_{5/2})_3\rightarrow(1s^22p_{1/2}2p_{3/2})_2$	2779.8	3.4929	1.16[12]		
$(1s2p_{3/2}^23d_{3/2})_3\rightarrow(1s^22p_{3/2}2p_{3/2})_2$	2770.9	3.4935	1.08[12]		
$(1s2p_{3/2}3d_{3/2})_3\rightarrow(1s^22p_{3/2}2p_{3/2})_2$	2770.2	3.9420	9.89[11]		
$(1s2s2p_{3/2}3s)_1\rightarrow(1s^22p_{1/2}2p_{3/2})_2$	2757.0	3.5155	8.15[11]		

autoionizing level relative to that of the heliumlike ground state, i.e., the energy of the captured electron. The emissivities of the berylliumlike dielectronic satellite lines are given by an expression similar to Eq. (8) except that N_{He} is replaced by N_{Li}. Atomic data necessary for computing the emissivities of the $1s2l3l'$ satellite lines in lithiumlike argon have been reported by a variety of authors [19–22]. The $1s3l3l'$ and $1s2l2l'3l''$ satellites lines have received much less attention in the literature, and we list the necessary atomic parameters for the strong lithiumlike and berylliumlike dielectronic satellites calculated with the HULLAC package in Tables V and VI, respectively.

Because the dielectronic recombination and electron-impact excitation processes sample different parts of the electron distribution, the intensity ratio of lines excited by dielectronic recombination and electron-impact excitation starting from the same initial state is sensitive to the electron temperature [18]. By taking the ratio

$$\varepsilon_{DR}/\varepsilon_{DE}=F_1F_2/C \tag{11}$$

the dependence on the ion density and on the electron density drops out. The electron temperature can thus be determined without knowledge of the relative ion abundance or the electron density.

III. EXPERIMENTAL RESULTS

Measurements were carried out on the PLT tokamak [23]. The spectra were recorded with a high-resolution Bragg crystal spectrometer in the Johann geometry used in earlier spectral measurements [24]. The instrument viewed the plasma along a line of sight through the horizontal midplane as illustrated in Fig. 1. The spectrometer employed a quartz $(11\bar{2}0)$ crystal with lattice spacing $d=2.4565$ Å, which was cylindrically bent to a radius $R=276$ cm. The resolving power of the instrument was $\lambda/\Delta\lambda=4500$, i.e., well above the Doppler-broadened linewidth of $\lambda/\Delta\lambda=1800$ for argon at 2 keV.

A measurement of the $K\beta$ emission of heliumlike argon is shown in Fig. 2. The data were accumulated by adding spectra from 23 Ohmically heating discharges with similar conditions, i.e., with central electron temperatures of 2.3 keV and central electron densities of 1.5×10^{13} cm^{-3}. Argon was introduced into the plasma at $t=800$ ms with a fast-switching gas valve in a 4-ms gas puff. The amount of argon was kept sufficiently low so as to not perturb the electron density and temperature by more than 10% during the gas puff. The radial electron temperature profile was determined as a function of time from the electron cyclotron emission, as illustrated in Fig. 3(a). A profile representative of the average temperature for the discharges and discharge times (800–1050 ms) during which spectroscopic data were accumulated is shown in Fig. 3(b). The spread of temperatures in this average is indicated by the vertical bars. The average central electron temperature for the measurements is 2.3 ± 0.2 keV.

Knowing the dispersion k of the spectrometer, the wavelength λ of a given line situated at a position N in

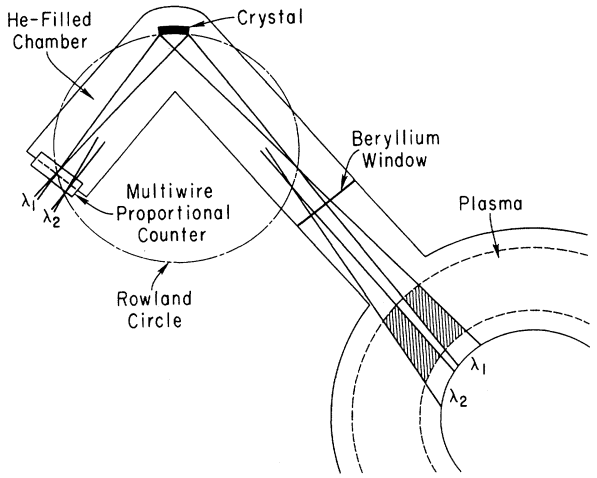

FIG. 1. Top view of the high-resolution Johann-type crystal spectrometer on the PLT tokamak. The spectrometer is viewing the horizontal midplane of the plasma. In accordance with Bragg's law, x rays incident upon the crystal are focused at different positions along the position-sensitive detector depending on their wavelength λ. A helium atmosphere is used to minimize x-ray absorption by air. Displacements perpendicular to the line of sight are exaggerated for clarity.

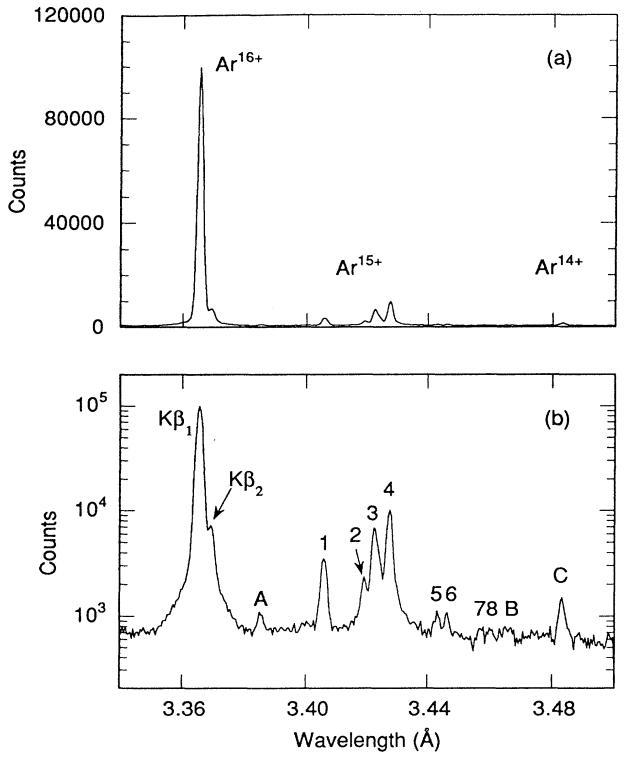

FIG. 2. $K\beta$ spectrum of argon: (a) linear and (b) logarithmic scale. The positions of features from heliumlike Ar^{16+}, lithiumlike Ar^{15+}, and berylliumlike Ar^{14+} are marked in (a). Individual features are labeled in(b) according to the notation used in the tables. The data were accumulated from 23 discharges.

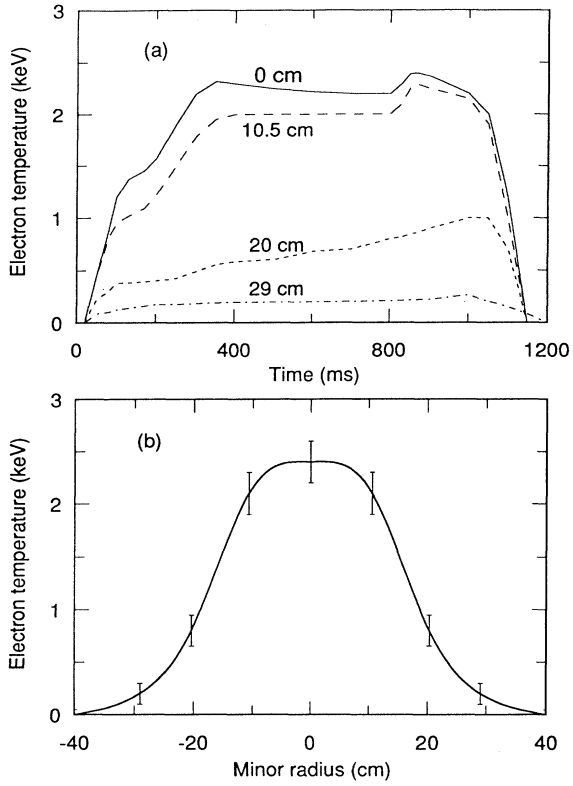

FIG. 3. Temporal evolution (a) and radial profile of the electron temperature (b) determined from the electron cyclotron emission. Four radial chords are shown in (a) for a typical discharge. Argon was injected at $t=800$ ms, resulting in a 10% rise in the electron temperature. Spectral data were accumulated throughout the discharge; data included in the present analysis were collected in the interval $t=800-1050$ ms. The profile in (b) represents the average electron temperature for the 23 discharges and times during which data for the present analysis were collected. The spread in electron temperature in this average is indicated by the vertical bars.

the spectrum can be measured relative to a calibration line of known wavelength using the relations

$$\lambda=2d\sin(\theta_0+\Delta\theta) \tag{12}$$

and

$$\Delta\theta=k(N_0-N)\,, \tag{13}$$

where θ_0 and N_0 are the Bragg angle and position of the calibration line. In our measurement we used the well-known positions of the Lyman-α lines of hydrogenic potassium for calibration. These lines are situated at 3.352 11 and 3.346 69 Å according to the calculations of Johnson and Soff [25].

Looking at Fig. 2(a) we note that the $K\beta_1$ line is the dominant spectral feature. Features from lithiumlike Ar^{15+} and berylliumlike Ar^{14+} are one to two orders of magnitude smaller in intensity, and some can only be seen by displaying the spectral data on a logarithmic scale [cf. Fig. 2(b)]. The smallest feature we identified is about three orders of magnitude less intense than $K\beta_1$.

The wide dynamic range allowed us to identify eight features in Ar^{15+}, labeled 1 through 8 in Fig. 2(b), that involved $1s2l3l'$ configurations. We also identified a feature, labeled A, that involved $1s3l3l'$ configurations. Moreover, we identified two features, labeled B and C, involving $1s2l2l'3l$ configurations in Ar^{14+}. A listing of the measured wavelengths is given in Tables I, V, and VI together with some of the transitions that contribute to each feature. Additional contributions to these features arise from dielectronic recombination with Ar^{16+}, as discussed in the next section, and are not listed. The statistical uncertainty in the measured position of each feature is less than 0.1 mÅ. An additional uncertainty arises from the absolute calibration, i.e., from the uncertainty in the position of the hydrogenic potassium lines used for calibration. The uncertainty in the absolute wavelength scale amounts to about 0.1 mÅ. The combined wavelength uncertainty is less than 0.2 mÅ.

IV. COMPARISON WITH THEORY

In the following we have made detailed comparisons of the measured spectrum with synthetic spectra based on the calculated atomic data for the $1s2l3l'$ and $1s3l3l'$ lithiumlike satellites and for the $1s2l2l'3l''$ berylliumlike satellites. The comparisons aid in line identification and assess the adequacy of the atomic data. In the final subsection we present a comparison of the predicted and measured intensity ratio of the two heliumlike lines $K\beta_1$ and $K\beta_2$.

A. $1s2l3l'$ satellites

Detailed atomic data pertaining to the dielectronic recombination via the $1s2l3l'$ intermediate states in Ar^{15+} were calculated by Chen [21] and Nilsen [22] using relativistic wavefunctions and allowing for configuration interaction. We use their data to construct the dielectronic satellite spectra shown in Figs. 4(a) and 4(b). In order to sum the intensities of unresolved lines each satellite is modeled with a width that equals the width of the $K\beta_1$ line as observed in the experiment. The vertical scale of the synthetic spectra is adjusted so that the intensity of feature 4 matches that of the measurement.

Comparing the synthetic dielectronic recombination spectra with the measurements we make several observations. First, the wavelengths entering the calculation of the synthetic spectra appear shifted from the measured values in a systematic way. The theoretical wavelengths of Chen need to be shifted by -0.9 mÅ, those of Nilsen by -2.0 mÅ, to obtain agreement in the position of key features with the measurements. This is demonstrated in Fig. 5 where we show a close-up comparison of the measured spectrum with the synthetic dielectronic satellite spectra shifted by -0.9 and -2.0 mÅ, respectively. A good match between the shifted and measured line positions is obtained. There is little variation among the predicted intensities of the strong features. For example, Chen [21] predicts the sum of all satellite lines contributing to feature 4 to be $F_2=10.3\times10^{13}$ s^{-1}, while Nilsen [22] predicts $F_2=10.1\times10^{13}$ s^{-1}. There are, however, significant variations in the predicted intensities of the weaker satellite lines, such as features 5 and 6 (cf. Fig. 5). The largest variation can be seen in the predicted intensities contributing to feature 1 [cf. Figs. 4(a) and 4(b)]. Here, Nilsen predicts $F_2=6.4\times10^{11}$ s^{-1} for a transition with wavelength $\lambda=3.4075$ Å, while Chen predicts $F_2=2.4\times10^{12}$ s^{-1} for a transition at $\lambda=3.4070$ Å and $F_2=8.2\times10^{11}$ s^{-1} for a transition at $\lambda=3.4079$ Å. The latter two transitions blend, resulting in a satellite feature five times larger than that predicted by Nilsen (cf. Fig. 5). Finally, we note that the synthetic dielectronic satellite spectra do not adequately describe the intensities of the features labeled 1 and 3. These two features are predominantly produced by transitions of the type $1s2s3p\rightarrow1s^22s$ excited by electron impact from the

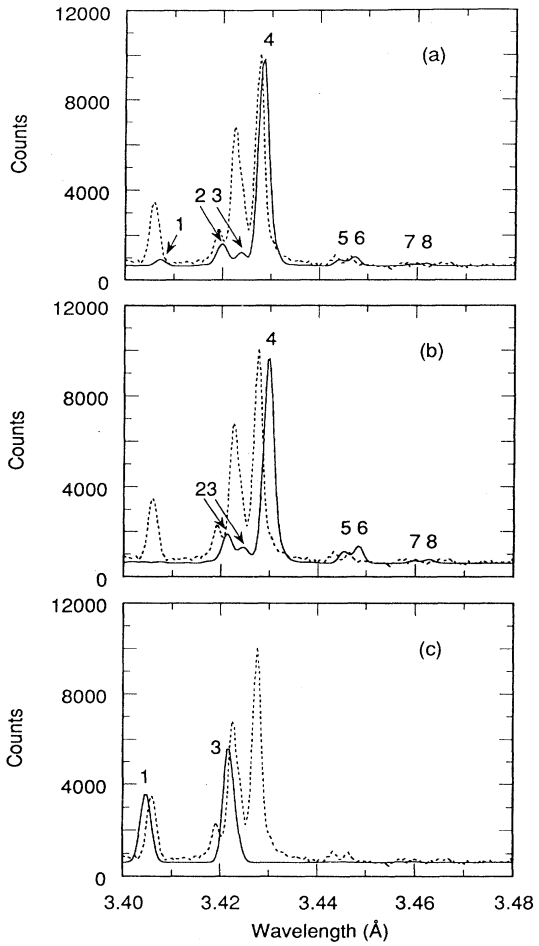

FIG. 4. Comparison between synthetic spectra (solid line) and measurement (dashed line) in the wavelength range 3.40–3.48 Å. The region contains transitions of the type $1s^22l$-$1s2l3l'$ excited by dielectronic recombination or electron collisions. Comparisons with the dielectronic satellite data from Chen [20] and Nilsen [21] are given in (a) and (b), respectively. The synthetic spectra are normalized to the feature labeled 4. A comparison with the collisional satellite data of Table I is given in (c). Here, the synthetic spectrum is normalized to the feature labeled 1.

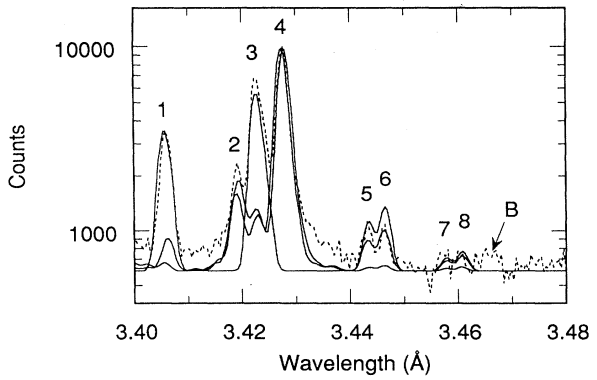

FIG. 5. Comparison between synthetic spectra (solid lines) and measurement (dashed line) in the wavelength range 3.40–3.48 Å. The synthetic spectra are the same as in Fig. 4 except that the data from Chen [20] were shifted by −0.9 mÅ, those from Nilsen [21] were shifted by −2.0 mÅ, and those from Table I by +1.3 mÅ to achieve better agreement with the measurement. A logarithmic scale is used to emphasize weak features. The feature labeled *B* is from berylliumlike Ar^{14+}.

ground level of lithiumlike ions and listed in Table I.

The spectral distribution and intensity of the collisional satellite lines are illustrated in Fig. 4(c), where we plotted the relevant theoretical atomic data given in Table I. The intensity of the synthetic spectrum was normalized to the measured intensity of feature 1. Like the predicted position of the dielectronic satellites, the position of the collisional satellites is shifted from the measured values. The shift is about +1.3 mÅ. This shift was applied to the synthetic spectrum in Fig. 5, where a good match between the line positions in the synthetic and measured spectra can be seen. Looking at Figs. 4 and 5 we find that the collisional satellites indeed describe the features not adequately accounted for by the dielectronic satellite lines.

The collisional satellites contribute in varying amounts also to those features produced mainly by dielectronic recombination. Such mixing of excitation processes makes a determination of the electron temperature based on Eq. (11) more difficult. Fortunately, the strongest dielectronic satellite feature, labeled 4, receives no contribution from collisional excitation processes, and we use the ratio of its intensity to that of $K\beta_1$ for determining the electron temperature. Using the collisional excitation rates listed in Table II and Chen's calculated values for the line strength F_2 of satellite feature 4, we compute the temperature variation of the intensity ratio of satellite feature 4 and $K\beta_1$ shown in Fig. 6(a). This agrees within experimental uncertainties with the measured ratio, as shown in the figure. Another way to quantify the agreement is to note that the temperature inferred from the ratio is $T_e = 2.10 \pm 0.02$ keV, where the uncertainties are purely statistical, while the peak temperature determined from the electron cyclotron emission and averaged for all spectral measurements is 2.3±0.2 keV. Looking at Eq. (9), it is not surprising that the electron temperature inferred from the satellite intensity is somewhat lower than the peak electron temperature measured from the

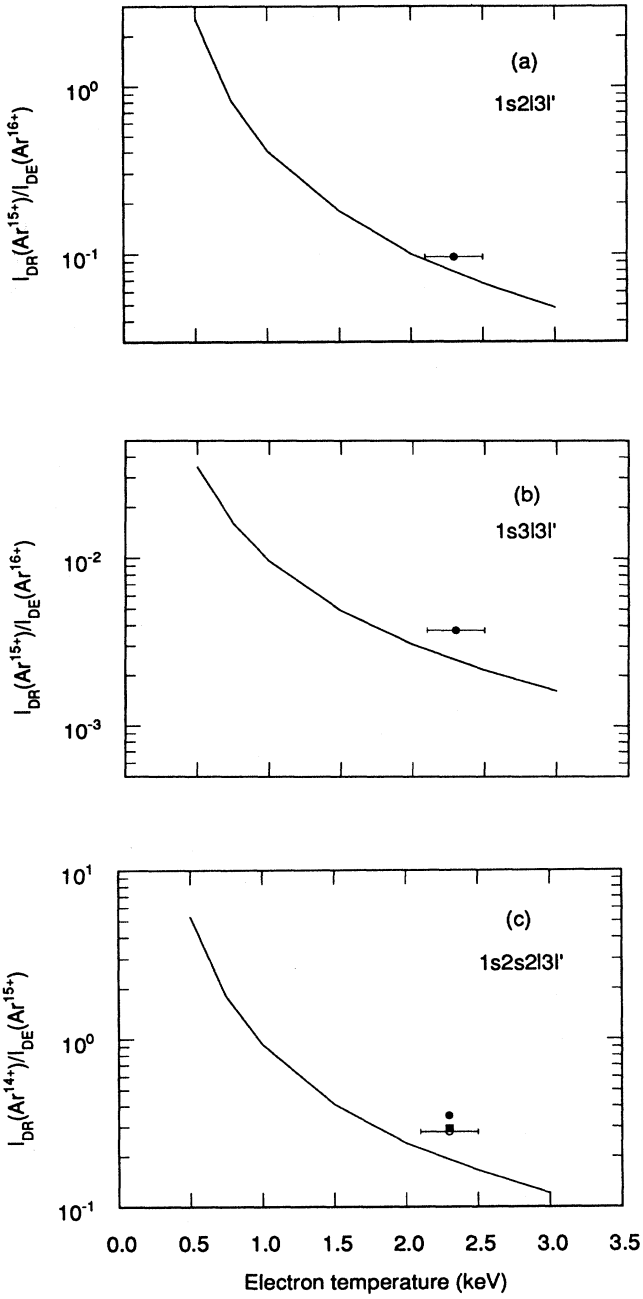

FIG. 6. Temperature dependence of the relative dielectronic satellite intensities and comparison with measured values. The intensity of the lithiumlike $1s2l3l'$ satellites comprising feature 4 relative to $K\beta_1$ is given in (a). The intensity of the lithiumlike $1s3l3l'$ satellites comprising feature *A* relative to $K\beta_1$ is given in (b). The intensity of the berylliumlike $1s2l2l'3l''$ satellites comprising feature *C* relative to the lithiumlike collisional satellite labeled 1 is given in (c). The measured ratios are indicated in (a) and (b) by solid circles. The measured ratio of features *C* and 1 is indicated in (c) by an open circle. Adjusting the measured intensity of feature 1 by a blend with a dielectronic satellite predicted by Nilsen [21] results in the value shown as a solid square. Adjusting the measured intensity of feature 1 by a blend with a dielectronic satellite predicted by Chen [20] results in the value shown as a solid circle.

electron-cyclotron emission, as the function $F_1(T_e)$, and thus recombination, peaks in the colder parts of the plasma.

B. $1s3l3l'$ satellites

An expanded view of the spectral region containing the $1s3l3l'$ dielectronic satellite lines is shown in Fig. 7. A synthetic spectrum constructed with the theoretical data listed in Table V and normalized to the intensity of feature A is shown for comparison with the measurement. Unlike the case for the $1s2l3l'$ satellites, the predicted position for the dominant $1s3l3l'$ feature matches the data well. An offset of only 0.2 mÅ is found. The calculations, however, underestimate the intensity of feature A relative to that of $K\beta_1$ by about 50%. This is seen when comparing the relative intensity predicted by Eq. (11) to the measured datum, as illustrated in Fig. 6(b). The temperature inferred from the measured ratio is 1.79±0.12 keV, which is well below the 2.3±0.2 keV expected from the electron cyclotron emission and the 2.10±0.02 keV inferred from the $1s2l3l'$ dielectronic satellite intensity (cf. Table VII). The latter difference is especially significant as the $1s3l3l'$ feature is populated in the same part of the plasma as the $1s2l3l'$ dielectronic satellites.

C. $1s2l2l'3l'$ satellites

An expanded view of the spectral region containing the $1s2l2l'3l''$ satellites from berylliumlike Ar^{14+} is shown in Fig. 8. The region contains several features, most of them weak, that cannot be described by either collisionally or dielectronically excited satellites from lithiumlike Ar^{15+} (cf. Fig. 5), but may instead be described by collisionally or dielectronically excited transitions in Ar^{14+}.

Electron collisions with the $1s^22s^2\,{}^1S_0$ ground state produce only one strong transition in Ar^{14+}, i.e., the transition $1s^22s^2\,{}^1S_0-1s2s^23p\,{}^1P_1$ (cf. Table I). Collisional excitation of the ground state also excites the $1s2s^23p\,{}^3P_1$ level (cf. Table IV). It, however, decays predominantly by autoionization, as the branching ratio for $1s$-$3p$ decay is a mere 0.9% (cf. Table I). Hence its expected intensity is a mere 0.1% that of the x-ray intensity resulting from the excitation of the $^1P_1$ level.

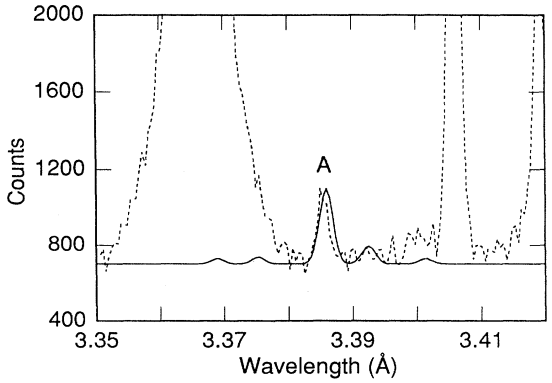

FIG. 7. Comparison between synthetic spectrum (solid line) and measurement (dashed line) in the wavelength range 3.35–3.42 Å. The region contains transitions of the type $1s^23l$-$1s3l3l'$ excited by dielectronic recombination. The synthetic spectrum is based on the dielectronic satellite data are from Table V and is normalized to the feature labeled A.

A feature corresponding to the predicted wavelength of the x ray emitted in the decay of the $1s2s^23p\,{}^1P_1$ level is found in our spectrum at 3.466 Å (Feature B). The feature, however, is weak and too broad to be comprised of a single line; definitive identification of this feature is, therefore, not possible.

Dielectronic recombination of a free electron with Ar^{15+} also excites levels that could contribute to the feature labeled B. These levels are indicated in Table VI, and a synthetic spectrum constructed from the $1s2l2l'3l''$ dielectronic satellite data is shown in Fig. 8. Here, the intensity of the synthetic spectrum was adjusted to match the intensity of the feature labeled C. According to the predictions, dielectronic satellite lines account for some but not all of feature B, intimating that

TABLE VII. Electron temperature inferred from the relative dielectronic satellite intensities. The temperature determined independently from the electron cyclotron emission is 2.3±0.2 keV.

Dielectronic satellites	Collisional line	Intensity ratio	Inferred temperature
$1s2l3l'$ (Feature 4)	$1s3p$ ($K\beta_1$)	0.096±0.001	2.10±0.002 keV
$1s3l3l'$ (Feature A)	$1s3p$ ($K\beta_1$)	0.0038±0.004	1.79±0.12 keV
$1s2l2l'3l''$ (Feature C)	$1s2s3p$[a] (Feature 1)	0.28±0.03	1.85±0.09 keV
$1s2l2l3l''$ (Feature C)	$1s2s3p$[b] (Feature 1)	0.30±0.03	1.80±0.09 keV
$1s2l2l3l''$ (Feature C)	$1s2s3p$[c] (Feature 1)	0.35±0.04	1.65±0.08 keV

[a]Line uncorrected for blends with dielectronic satellites.
[b]Line corrected for blends with satellite transitions using the theoretical values from Ref. [21].
[c]Line corrected for blends with satellite transitions using the theoretical values from Ref. [20].

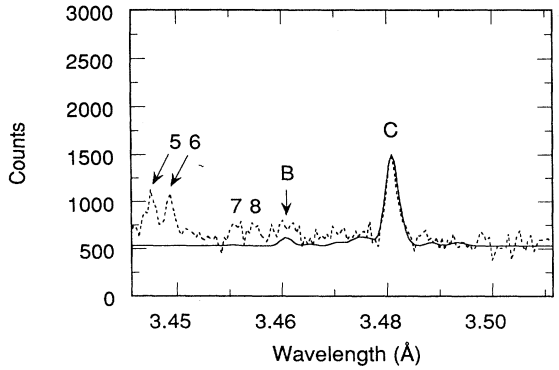

FIG. 8. Comparison between synthetic spectrum (solid line) and measurement (dashed line) in the wavelength range 3.44–3.51 Å. The region contains transitions of the type $1s^2 2l 2l'$-$1s 2l 2l' 3l''$ in berylliumlike Ar^{14+} excited by dielectronic recombination or electron collisions. The synthetic spectrum is based on the dielectronic satellite data from Table VI and is normalized to the feature labeled *C*. The feature labeled *B* may be enhanced by the collisionally excited resonance transition $1s^2 2s^2\ ^1S_0$–$1s 2s^2 2p\ ^1P_1$ in berylliumlike Ar^{14+}. The features labeled 5, 6, 7, and 8 are from $1s^2 2l$-$1s 2l 3l'$ transitions in lithiumlike Ar^{15+}.

the radiative decay of the collisionally excited $1s 2s^2 3p\ ^1P_1$ level indeed contributes to the feature.

The atomic data for dielectronically excited transitions given in Table VI appear to adequately describe the feature labeled *C*. A good match with the measured position is achieved without shifting the predicted wavelengths. However, the predicted intensity appears to underestimate the data although some caveats are necessary. Using Eq. (11) we plot in Fig. 6(c) the predicted intensity of feature *C* relative to the intensity of the two collisional satellite lines in lithiumlike Ar^{15+} that contribute to the feature labeled 1 (cf. Table I). Before comparing this prediction with the measured ratio we note that feature 1 is not exclusively comprised of the two collisionally excited lines listed in Table I but consists in part of transitions excited by dielectronic recombination (cf. Figs. 4 and 5). The exact contribution arising from dielectronic satellites, however, is uncertain. As noted above, the fraction due to dielectronic recombination is predicted five times as high by Chen as by Nilsen. We subtract the contributions from dielectronic satellites to feature 1 before taking the quotient with the intensity of feature *C*. The results are shown in Fig. 6(c). The first, where no adjustment for dielectronic satellite contributions is made, affords the best agreement with the predicted ratio. The electron temperature inferred from this ratio is 1.89±0.09 keV. The second, where we subtracted the dielectronic satellite contributions predicted by Nilsen from the measured intensity of feature 1, differs incrementally more from the predicted ratio, and the inferred electron temperature is 1.80±0.09 keV (cf. Table VII). The third, where we subtracted the dielectronic satellite contributions predicted by Chen from the intensity of feature 1, disagrees the most with the predicted ratio. The inferred electron temperature is 1.65±0.08 keV. The predictions for the berylliumlike satellites thus match the observed data best if we rely on Nilsen's $1s 2l 3l'$ predictions or do not account for blends. While both values are well below the peak value of 2.3±0.2 determined from the electron cyclotron emission or the value of 2.10±0.02 inferred from the lithiumlike satellite intensity, this is not unreasonable considering that berylliumlike satellites are likely to be produced in a plasma region colder than that producing lithiumlike satellites. If we rely on Chen's predictions, we must conclude that the line strengths for the berylliumlike satellites are predicted too small or the excitation rates of the lithiumlike collisional satellites too large. The present data do not allow us to discriminate between these two possibilities.

Looking at Fig. 8 we note several other features in the synthetic spectrum that might explain some of the features seen in the measured spectrum. These features, however, are weak and comparable to the noise level of the data. Identification of these features is thus not possible.

D. The Ar^{16+} resonance and intercombination lines

Collisional excitation of the $1s^2\ ^1S_0$ ground state in heliumlike Ar^{16+} predominantly populates the $1s 3p\ ^1P_1$ singlet level. The excitation rate for the triplet level is 3–10 times less, depending on the electron temperature (cf. Table II). Moreover, the triplet level decays back to the ground state only 17% of the time compared to 95% for the singlet level. The intensity of $K\beta_2$ thus is markedly less than that of $K\beta_1$.

At 2.3 keV our calculations predict that the intensity of $K\beta_2$ is a mere 2.3% that of $K\beta_1$ (cf. Table I). This prediction, however, does not match the measurements. In Fig. 9 we show an expanded view of the spectral region containing the Ar^{16+} $K\beta$ lines. A large discrepancy between the predicted and measured intensity of $K\beta_2$ is seen. In fact, the measured relative intensity is two times larger than predicted by the collisional excitation rate, as summarized in Table VIII. In determining the relative intensity of $K\beta_2$ we subtracted the background level arising from the quasi-Lorentzian line shape of $K\beta_1$. A simi-

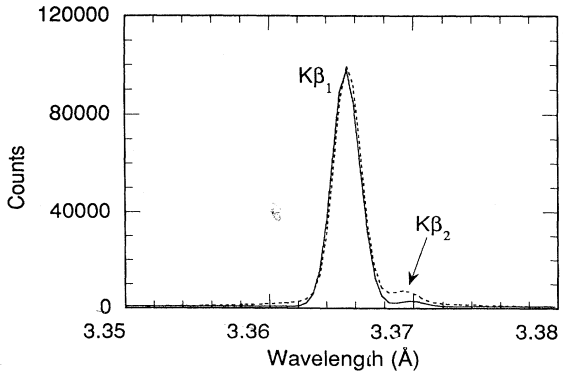

FIG. 9. Comparison between calculated (solid line) and measured (dashed line) intensities of the heliumlike $K\beta$ lines. The calculated ratio is normalized to the measured intensity of $K\beta_1$.

TABLE VIII. Comparison of measured and calculated intensity ratio R of $K\beta_1$ and $K\beta_2$ in Ar^{16+}.

Ion	T_e (keV)	R^{expt}	R^{theor}
Ar^{16+}	2.3	0.048	0.023
Fe^{24+}	2.8	0.28[a]	0.13[a]

[a]From Ref. [4].

lar discrepancy was found earlier in the measurement of the relative intensities of $K\beta_2$ and $K\beta_1$ in heliumlike Fe^{24+} [4]. The ratio predicted with similar theoretical methods was 13%, while the measured ratio was 28% (cf. Table VIII).

The intensity ratio depends on the electron temperature, as illustrated in Fig. 10. The ratio drops by a factor of 3 between 500 and 3000 eV. This variation, together with the uncertainty in the measured electron temperature, however, is not sufficient to explain the discrepancy between the predicted and measured ratio. A temperature nearly an order of magnitude lower than measured would be required to achieve agreement.

The measured intensity of $K\beta_2$ may be enhanced by three processes unaccounted for in our prediction. First, radiative cascades from higher levels may significantly enhance the population of the triplet level. While radiative cascades may also feed $K\beta_1$, the effect is relatively larger for the triplet level. This was demonstrated in several analyses of the relative intensities of the singlet and triplet level populations in the heliumlike $K\alpha$ lines [26]. No such radiative cascade processes were considered in our predictions. Second, $K\beta_2$ may blend with lithiumlike dielectronic satellite lines of the type $1s^2nl$-$1s3lnl'$ with $n \geq 4$. Such satellites are situated on the long-wavelength side of $K\beta_1$ and are closer to $K\beta_1$ than the $1s3l3l'$ satellites considered above. While some of the so-called high-n satellites may also blend with $K\beta_1$, their impact could be relatively larger on $K\beta_2$ than on $K\beta_1$. The significance of high-n satellites has already been demonstrated in analysis of the heliumlike $K\alpha$ spectra [10–13]. Because $K\beta_2$ is a weak feature, any enhancement from blends with weak high-n satellites could be substantial and make a large difference. Third, radiative and dielectronic recombination of hydrogenic Ar^{17+} preferentially enhances the intensity of $K\beta_2$ over $K\beta_1$. The amount of Ar^{17+} is not known. However, a significant amount of Ar^{17+} may be present considering the observation of hydrogenic K^{18+} used in the calibration of the spectral measurements. Whether the inclusion of these processes will indeed enhance the intensity of $K\beta_2$ relative to the observed level needs to be tested in future investigations.

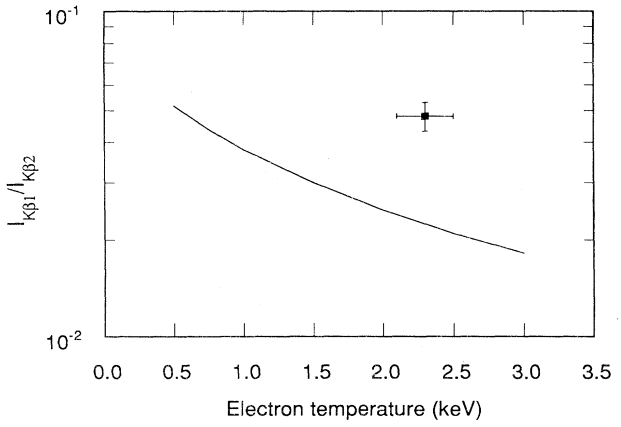

FIG. 10. Predicted temperature dependence of the relative intensities of the heliumlike $K\beta$ lines and comparison with the measured value. The predicted intensities are based on the relative collisional excitation rates of Table II and do not include cascade contributions or blends with high-n satellites.

V. DISCUSSION

We have presented measurements of the $K\beta$ spectra of heliumlike argon from the PLT tokamak. A detailed comparison with synthetic spectra that included contributions from dielectronic satellite lines and the emission from lines excited by electron impact was made to aid line identification and test theoretical predictions. Using these predictions we were able to identify all distinct features in the spectrum including the $1s3l3l'$ dielectronic satellites, and predicted wavelengths were found to agree within 2 mÅ with the measured values. The theoretical atomic data of the strong dielectronic satellite transitions appear to describe the measurements well. A measure of how well the theoretical data reproduce the measurements is given by the electron temperature inferred from the relative ratio of dielectronic satellite and appropriate collisional satellite lines. The temperature inferred from the relative intensity of the strongest $1s2l3l'$ dielectronic satellite feature matched the measured peak plasma temperature within experimental uncertainties, as summarized in Table VII. In fact, most calculations predict similar values for the line strengths of the strongest dielectronic satellites. The intensity of the weaker satellites, however, is much more uncertain. Different calculations differ among each other significantly. This is reflected in the temperature inferred from the relative intensity of the $1s2l2l3l'$ berylliumlike dielectronic satellite feature. A blend with a weak $1s2l3l'$ dielectronic satellite whose predicted intensity varies within a factor of 5 among different calculations makes the inferred temperature uncertain within a significant range, as summarized in Table VII. Similarly, the relative intensity of the $1s3l3l'$ satellites appears substantially underestimated, resulting in an inferred temperature well below the value inferred from the $1s2l3l'$ satellites (cf. Table VII).

In our analysis we have emphasized individual features. Using an analysis that aims to achieve an overall best fit to the dielectronic satellites would average over some of the disagreements noted and would result in a reliable value for the inferred electron temperature that agrees with the temperature measured with nonspectroscopic means. The $K\beta$ spectra of heliumlike ions can thus be used for diagnostic purposes, complementing the

diagnostic utility of the heliumlike $K\alpha$ spectra in low-density astrophysical, solar, and magnetic-fusion plasmas.

The relative collisional excitation rates for the collisional satellites match the measurements within the experimental precision. The fact that all collisional satellite features are blended to some degree with dielectronically excited features limits, however, the experimental precision with which a comparison can be made.

By contrast to the $1s2l3l'$ collisional satellites, we can make a definitive comparison between predictions and observations in the case of the heliumlike lines $K\beta_1$ and $K\beta_2$. Here, we find that the relative intensity of $K\beta_2$, which proceeds from a triplet level, is underestimated. Cascade contributions from high-lying levels, which are not included in the predictions, may disproportionately enhance $K\beta_2$. However, a factor of 2–3 enhancement is needed for the predictions to match the observed ratio, which may not be entirely accomplished by including cascades. Dielectronic and radiative recombination of hydrogenic Ar^{17+} also enhances $K\beta_2$ relative to $K\beta_1$. A measurement of the relative abundance of Ar^{17+} would be needed for proper inclusion of this excitation process in future models.

High-n dielectronic satellite transitions of the type $1s3pnl \rightarrow 1s^2nl$ with $n \geq 4$ situated at the position of the $K\beta_2$ line may also explain, at least in part, the large observed intensity of $K\beta_2$. Such transitions have been observed on the long-wavelength side of the singlet transition in the heliumlike $K\alpha$ spectra. Their presence is likely given our observation of a feature formed by $1s3l3l'$ transitions. However, the intensity of the $1s3l3l'$ satellites in feature A is only 5% that of $K\beta_2$ so that a large enhancement of $K\beta_2$ by high-n satellites seems less likely. Using electron-beam excitation to produce the $K\beta$ transitions separately from the high-n dielectronic satellites [27] it may be possible to disentangle the relative contributions to the $K\beta_2$ feature. Precise knowledge of these contributions is of special importance in density determinations of ICF plasmas from the Stark broadening of the heliumlike $K\beta$ lines. Significant broadening of the $K\beta$ feature from high-density plasmas by the $1s3l3l'$ satellites has already been demonstrated [8,9]. Additional broadening may arise from the presence of high-n satellites, especially at electron temperatures lower than in our measurement. Resolving the discrepancy between theory and measurement of the relative intensity of $K\beta_2$ in future investigations could thus have significant implications for the diagnostic use of the $K\beta$ spectra in high-density plasmas.

ACKNOWLEDGMENTS

The support received by Tom Gibney and Janet Felt is greatly acknowledged. This work was performed under the auspices of the U.S. DOE under Contract No. W-7405-ENG-48 by the Lawrence Livermore National Laboratory and under Contract No. DE-AC02-76-CHO-3073 by the Princeton Plasma Physics Laboratory.

[1] K. W. Hill, P. Beiersdorfer, M. Bitter, E. Fredrickson, S. von Goeler, H. Hsuan, K. McGuire, N. R. Sauthoff, S. Sesnic, and J. E. Stevens, in *Course and Workshop on Basic and Advanced Diagnostic Techniques for Fusion Plasmas, Varenna, Italy, 1986,* edited by P. Stott *et al.* (Office for Official Publications of the European Communities, Luxembourg, 1987), Vol. I, p. 169; E. Källne, in *Physics of Highly Ionized Atoms,* NATO Advanced Study Institute, Series B: Physics, Vol. 201, edited by R. Marrus (Plenum, New York, 1989), p. 245.

[2] E. Källne, J. Källne, J. Dubau, E. S. Marmar, and J. E. Rice, Phys. Rev. Lett. **52**, 2245 (1984).

[3] J. E. Rice, E. S. Marmar, E. Källne, and J. Källne, Phys. Rev. A **35**, 3033 (1987).

[4] A. J. Smith, M. Bitter, H. Hsuan, K. W. Hill, S. von Goeler, J. Timberlake, P. Beiersdorfer, and A. Osterheld, Phys. Rev. A **47**, 3073 (1993).

[5] V. A. Boiko, S. A. Pikuz, U. I. Safronova, and A. Ya. Faenov, Mon. Not. R. Astron. Soc. **185**, 789 (1978); P. G. Burkhalter, J. Shiloh, A. Fisher, and R. D. Cowan, J. Appl. Phys. **50**, 4532 (1979).

[6] A. Hauer, K. B. Mitchell, D. B. van Hulsteyn, T. H. Tan, E. J. Linnebur, M. Mueller, P. C. Kepple, and H. R. Griem, Phys. Rev. Lett. **45**, 1495 (1980); B. Yaakobi, S. Skupsky, R. L. McCrory, C. F. Hooper, H. Deckman, P. Bourke, and J. M. Soures, *ibid.* **44**, 1072 (1980); J. D. Kilkenny, Y. Lee, M. H. Key, and L. G. Lunney, Phys. Rev. A **22**, 2746 (1980).

[7] B. A. Hammel, C. J. Keane, D. R. Kania, J. D. Kilkenny, R. W. Lee, R. Pasha, R. E. Turner, and N. D. Delameter, Rev. Sci. Instrum. **63**, 5017 (1992); B. A. Hammel, C. J. Keane, M. D. Cable, D. R. Kania, J. D. Kilkenny, R. W. Lee, and R. Pasha, Phys. Rev. Lett. **70**, 1263 (1993); B. A. Hammel, C. J. Keane, T. R. Dittrich, D. R. Kanis, J. D. Kilkenny, R. W. Lee, and W. K. Levedahl, J. Quant. Spectrosc. Radiat. Transfer **51**, 113 (1994).

[8] C. J. Keane, B. A. Hammel, D. R. Kania, J. D. Kilkenny, R. W. Lee, A. L. Osterheld, L. J. Suter, R. C. Mancini, C. F. Hooper, Jr., and N. D. Delameter, Phys. Fluids B **5**, 3328 (1993).

[9] R. C. Mancini, C. F. Hooper, N. D. Delameter, A. Hauer, C. J. Keane, B. A. Hammel, and J. K. Nash, Rev. Sci. Instrum. **63**, 5119 (1992).

[10] K. J. H. Phillips, F. P. Keenan, L. K. Harra, S. M. McCann, E. Rachlew-Källne, J. E. Rice, and M. Wilson, Nucl. Instrum. Methods Phys. Res. Sect. B **79**, 78 (1993).

[11] F. Bely-Dubau, P. Faucher, L. Steenman-Clark, M. Bitter, S. von Goeler, K. W. Hill, C. Cmahy-Val, and J. Dubau, Phys. Rev. A **26**, 3459 (1982).

[12] M. Bitter, S. von Goeler, K. W. Hill, R. Horton, D. Johnson, W. Roney, N. Sauthoff, E. Silver, and W. Stodiek, Phys. Rev. Lett. **47**, 921 (1981).

[13] F. Bombarda, R. Giannella, E. Källne, G. J. Tallents, F. Bely-Dubau, P. Faucher, M. Cornille, J. Dubau, and A. H. Gabriel, Phys. Rev. A **37**, 504 (1988).

[14] F. Bely-Dubau, J. Dubau, P. Faucher, and A. H. Gabriel,

Mon. Not. R. Astron. Soc. **198**, 239 (1982).
[15] M. Klapisch, Comput. Phys. Commun. **2**, 239 (1971); M. Klapisch, J. L. Schwob, B. S. Fraenkel, and J. Oreg, Opt. Soc. Am. **61**, 148 (1977).
[16] A. Bar-Shalom, M. Klapisch, and J. Oreg, Phys. Rev. A **38**, 1773 (1988).
[17] J. Oreg, A. Bar-Shalom, W. H. Goldstein, and M. Klapisch, Phys. Rev. A **44**, 1750 (1991).
[18] A. H. Gabriel, Mon. Not. R. Astron. Soc. **160**, 99 (1972).
[19] C. P. Bhalla and T. W. Tunnell, J. Quant. Spectrosc. Radiat. Transfer **32**, 141 (1984).
[20] L. A. Vainshtein and U. I. Safronova, Phys. Scr. **31**, 519 (1985).
[21] M. H. Chen, At. Data Nucl. Data Tables **34**, 301 (1986).
[22] J. Nilsen, At. Data Nucl. Data Tables **38**, 339 (1988).
[23] J. Hosea, R. Goldston, and P. L. Colestock, Nucl. Fusion **25**, 1155 (1985).
[24] P. Beiersdorfer, M. Bitter, S. von Goeler, S. Cohen, K. W. Hill, J. Timberlake, R. S. Walling, M. H. Chen, P. L. Hagelstein, and J. H. Scofield, Phys. Rev. A **34**, 1297 (1986); P. Beiersdorfer, M. Bitter, S. von Goeler, and K. W. Hill, *ibid.* **40**, 150 (1989).
[25] W. R. Johnson and G. Soff, At. Data Nucl. Data Tables **33**, 405 (1985).
[26] M. Bitter, K. W. Hill, M. Zarnstorff, S. von Goeler, R. Hulse, L. C. Johnson, N. R. Sauthoff, S. Sesnic, and K. M. Young, Phys. Rev. A **32**, 3011 (1985); M. Bitter, H. Hsuan, V. Decaux, B. Grek, K. W. Hill, R. Hulse, L. A. Kruegel, D. Johnson, S. von Goeler, and M. Zarnstorff, *ibid.* **44**, 1796 (1991).
[27] P. Beiersdorfer, M. B. Schneider, M. Bitter, and S. von Goeler, Rev. Sci. Instrum. **63**, 5029 (1992).